npj | Materials Degradation

www.nature.com/npjmatdeg

ARTICLE OPEN

How build angle and post-processing impact roughness and corrosion of additively manufactured 316L stainless steel

Michael A. Melia[1]✉, Jesse G. Duran[1], Joshua R. Koepke[1], David J. Saiz[1], Bradley H. Jared[1] and Eric J. Schindelholz[2]

Additively manufactured austenitic stainless steels exhibit numerous microstructural and morphological differences compared to their wrought counterparts that will influence the metals corrosion resistance. The characteristic as-printed surface roughness of powder bed fusion (PBF) stainless steel parts is one of these morphological differences that increases the parts susceptibility to localized corrosion. This study experimentally determines the average surface roughness and breakdown potential (E_b) for PBF 316L in 6 surface finished states: as-printed, ground with SiC paper, tumble polished in abrasive media, electro-polished, chemically passivated, and the application of a contour/re-melt scan strategy. In general, a smaller average surface roughness led to a larger E_b. The smoothest surface treatments, ground and electro-polished conditions, led to E_b near the materials limit (~+1.0 $V_{Ag/AgCl}$) while all other surface treatments exhibited significantly lower E_b (~+0.3 $V_{Ag/AgCl}$) The build angle was also shown to impact surface roughness, where surfaces at high angles from the build direction resulted in larger roughness values, hence lower E_b.

npj Materials Degradation (2020)4:21 ; https://doi.org/10.1038/s41529-020-00126-5

INTRODUCTION

Most investigations into the corrosion behavior of powder-based additively manufactured (AM) metal parts aim to compare AM parts to a wrought counterpart, focusing on how susceptibility to local corrosion initiation can be increased from the atypical microstructural features and processing defects found in AM metals[1–16]. A recent review by Sander et al. summarizes how some of these features can cause higher susceptibility toward the initiation of local corrosion than others and in relation to a wrought counterpart[17]. For instance internal part porosity, a common processing defect, has received significant attention and was shown to serve as preferential site for corrosion initiation in chloride solutions by several authors[7,9,18–22]. Schaller et al. and Melia et al. empirically showed corrosion to preferentially occur at lack of fusion pores for powder-based AM austenitic stainless steels, leading to a reduction in breakdown potential (E_b) compared to areas excluding this porosity[7,20]. Several other examples of microstructural features and processing defects that have been investigated are; nanoscale oxides/inclusions[7,20,23,24], solute segregation (i.e. cell boundaries, melt pool boundaries)[7,13,22–29], texture and grain character[29], residual stresses[3,30,31], surface roughness[18,20,32–35], and porosity[7,9,18–22].

Another result of the powder-based AM processes is high surface roughness, a major concern for AM part reliability and a characteristic that has received minimal attention with regards to its impact on corrosion. Currently, most of the aforementioned corrosion studies investigate samples in a ground surface condition (planar grinding) with very few addressing how the as-printed AM surfaces impact corrosion behavior[18,20,32–35]. The work by Cabrini et al. showed a reduction in corrosion resistance and crevice potential for the as-printed surface of the 625 Ni alloy when compared to a polished surface in 0.6 M NaCl solution[18]. The polished AM parts improved corrosion resistance was stated to stem from a decrease in surface porosity, which served as sites for crevice corrosion, and from the polishing imparting a less defective passive oxide film.

Similar studies have investigated the impact of surface roughness on the pitting behavior of stainless steels, mostly via altering the roughness by changing polishing grit sizes[20,36–39]. The consensus from these roughness/corrosion studies was larger roughness values lead to a higher frequency of metastable pitting, stemming from more heterogeneous pit initiation sites (at non-metallic inclusions, high aspect ratio surface features, etc.) on the rougher surface[20,36]. For an AM parts surface the large roughness, high aspect ratio, and tortuous features will exacerbate this pit initiation frequency effect as compared to a ground or machined surface[18,40]. Also the development of aggressive solution chemistries at the bottom of the crevice-like/nodular features will increase the likelihood a pit will stabilize and propagate when compared to a smooth surface without these asperities[9,41].

The tortuous surface roughness common for all metallic parts made by powder-based AM techniques has been shown to increase susceptibility to mechanical and environmental stressors with the potential for premature failure[40,42–44]. Bagehorn et al. shows the added susceptibility to mechanical stressors for a Ti alloy where the large roughness associated with the as-printed AM surface caused a reduction in fatigue life compared to an AM specimen with a machined surface[40]. For the powder bed fusion (PBF) technique these sharp, high aspect ratio, nodular features are formed by the partial melting and adherence of powder adjacent to the outer most edge of a build layer, as shown in Fig. 1, leading to "cling-on" features roughly the size of the powder used, 10–45 µm for PBF[45,46]. The density of partly melted and adhered powder will depend on the surface's angle with respect to the build plate with larger angles and overhung surfaces often exhibiting more partially melted powder adherence[33,45,47–49]. This leads to a difference in roughness and tortuosity with respect to build orientation/surface build angle as well as processing parameters[50–56].

Recent studies address how best to quantify these powder-based AM part's rough surfaces, unique when compared to conventional materials surface finishes with many undercut, sharp,

[1]Center for Materials Science and Engineering, Sandia National Laboratories, PO Box 5800, Albuquerque, NM 87185, USA. [2]Department of Materials Science and Engineering, The Ohio State University, Columbus, OH 43210, USA. ✉email: mamelia@sandia.gov

Published in partnership with CSCP and USTB

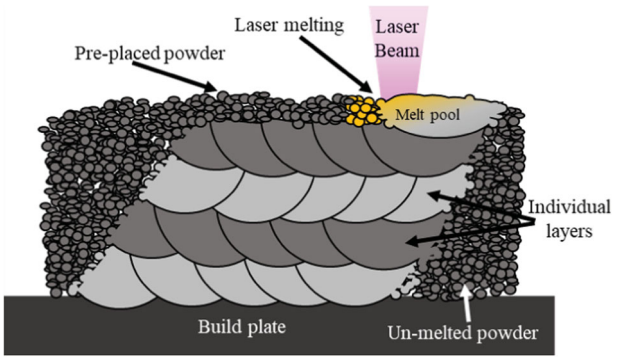

Fig. 1 The powder bed fusion process. A cross-sectional schematic view of the layer by layer powder bed fusion (PBF) process.

and overhung features[47,52]. The study by Cabanettes et al. investigated as-printed surfaces with common metrology tools, such as the stylus contact and optical profilometry methods[52]. The stylus technique was decidedly insufficient for characterizing the roughness of as-printed surfaces because of data lost to stylus artifacts. In contrast, optical profilometry was able to qualitatively and quantitatively differentiate most high aspect ratio features of the AM surfaces. The areal arithmetic mean height (S_a) was shown to increase as the sample orientation (build angle) increased and transferred to down facing surfaces. That said, optical profilometry is limited by line of sight effects, concealing sharp undercut features that will be critical to describing stress and environmental stressors on the as-printed surface[57]. Recent studies by Fox et al. and Kim et al. use x-ray computed tomography to more accurately measure the entire as-printed surface, including these sharp undercut regions[57,58].

Many studies have been performed attempting to alleviate the large roughness observed on AM parts with several polishing approaches being explored:

- Electropolishing[38,59–67]
- Laser surface modifications (re-melting, shock peening, etc.)[68–76]
- Mechanical surface finishing (planar polishing, tumble polishing, etc.)[20,33,35,40,43,44,77–82]
- Chemical polishing[83,84]
- Investigating multiple techniques, separate and combined[78,85,86]

All techniques showed reductions in surface roughness of the AM parts, yet an issue for many of them is their inability to effectively polish a complex shaped part. Electropolishing presents itself as a sound method to polish complex shapes, with current studies by Urlea et al. on building customized cathodes adjacent to an AM part to improve polishing efficiency[64,65]. However, uniform polishing rates will remain an issue for small, high aspect ratio features that require tight tolerances. The inability to maintain both finish and surface accuracy is a general challenge with any polishing process, regardless of the geometrical complexity[47,72,78].

No studies systematically investigate surface roughness's impact on an AM metal parts susceptibility to localized corrosion. There are also few studies that show the impact surface finish treatments have on AM metal parts and correlates these treatments to the parts local corrosion susceptibility. The main thrusts of this work will demonstrate how the surface roughness of an as-printed PBF 316L part depends on sample geometry and provide an explanation for how this roughness impacts susceptibility to local corrosion initiation. Additionally, five different surface finish treatments will show how they can reduce this susceptibility to local corrosion initiation. Five different surface finish treatments were performed on the as-printed surface of PBF 316L parts to reduce roughness and/or reduce susceptibility to local corrosion initiation.

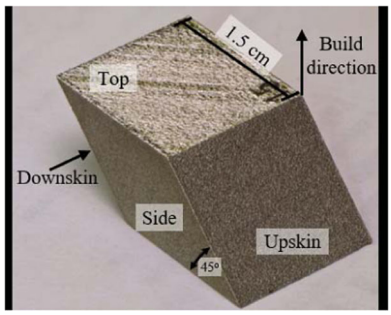

Fig. 2 Sample design. An optical image of the parallelepiped prism used for this study.

Table 1. Surface finishing treatments.

As-printed
Passivated
Contour scan strategy/surface re-melting
Tumble polished
Electropolished
Ground (planar grinding/polishing)
Wrought sample after grinding

RESULTS AND DISCUSSION

Sample geometry and surface finish treatments

The samples for this study were made using a PBF technique with 316L stainless steel powder whose processing parameters are elaborated in the "Methods" section. To investigate the dependence of corrosion behavior on sample orientation (build angle), samples were built in the shape of parallelepiped prisms, as shown in Fig. 2. The build angles are labeled in Fig. 2 as top (normal is parallel to the build direction), side (normal is perpendicular to the build direction), upskin (normal is 45° from the build direction), and downskin (normal is 135° from the build direction). Similar shapes have been utilized in previous studies to show roughness dependence on build angle[52,53,78]. Additionally the parallelepiped prism provides an overhung surface without support material and large flat surfaces making it easy to perform electrochemical experiments.

The list in Table 1 summarizes the six surface conditions under which the PBF parallelepiped prism samples were examined in this study. Specific process parameters regarding each surface finish treatment can be found in the "Methods" section.

Surface morphology and microstructure

Secondary electron images of the as-printed, electropolished, tumble polished, and contour scan strategy with a top surface re-melt step surfaces are shown Fig. 3 for two of the surface orientations, top and side. The as-printed top surfaces, Fig. 3a, exhibited PBF-typical characteristics with distinct melt tracks, partially fused power particles and balling. Electropolishing to an approximate depth of 13 um below the lowest point of the as-printed surface, eliminated these partially fused features, producing a smooth surface Fig. 3b. Tumble polishing, Fig. 3c, resulted in partial removal and flattening of the highest asperities. The material removal from tumble polishing, with proper optimization could lead to smoother and less tortuous surface roughness, however these optimizations are out of the scope of this work. Comparing Fig. 3a, d, the contour/laser re-melting process used a second laser scan across the entire top surface, and contour passes around the perimeter of each layer area. This produced

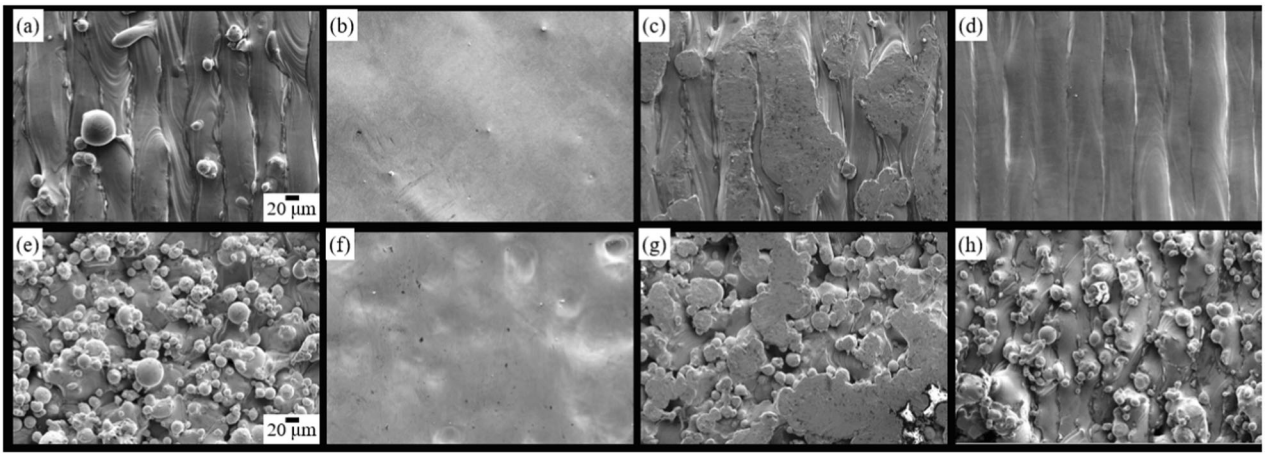

Fig. 3 Images of the sample surfaces. Secondary electron images of the surfaces for the **a**–**d** top and **e**–**h** side orientations with varying surface finishes; **a**, **e** as-printed, **b**, **f** electro-polished, **c**, **g** tumble polished, **d**, **h** contour scan/re-melting.

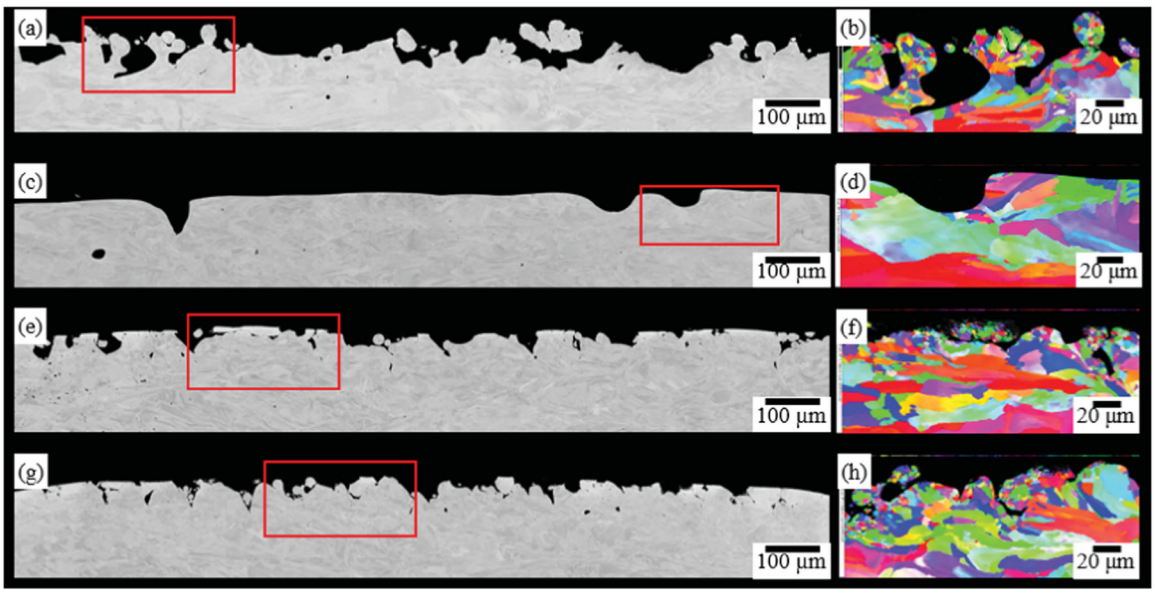

Fig. 4 Images and EBSD maps of surface cross-sections. BSE images (**a**, **c**, **e**, and **g**) and inverse pole figure maps (**b**, **d**, **f**, and **h**) of the surfaces in cross-section for the side orientation. The four surface finishes are shown in **a**, **b** as-printed, **c**, **d** electro-polished, **e**, **f** tumble polished, **g**, **h** contour scan/re-melting.

smoother top surface melt tracks than the single pass strategy with minimal partially fused powder particles. It also improved the side surface, again reducing the quantity of partially used powder.

The as-printed side surfaces were expectedly much rougher than the top surfaces and decorated with a multitude of partially fused powder particle cling-ons, Fig. 3e, h. The contour scan strategy was not as effective as it was on the top surface, but it did appear to reduce the cling-on particle number density Fig. 3h. Electropolishing the as-printed side orientation produced smooth surfaces, in Fig. 3f, similar to the electropolished top surface in (b) but with more dimpling. The dimpling was likely caused by the much rougher starting surface and deeper cavities. Tumble polishing had the same effect on the side surfaces, in Fig. 3g, as it did on the top surface (c). The upskin and downskin as-printed surfaces shown in Supplementary Figure 1 were similar in appearance to the sides but with different degrees of roughness. Electropolishing and tumble polishing of these surfaces produced similar results to the sides as well. A PBF 316L planar ground surface is shown in Supplementary Fig. 1(i), this surface morphology was the same for all build angles and when comparing wrought to PBF.

Cross sections of all sample surface treatments and along each build angle were imaged using backscattered electron (BSE) microscopy and electron backscattered diffraction (EBSD), shown in Fig. 4 for the side orientation. All other cross-sectioned specimens with different surface finishes and orientations are presented in the Supplementary Figs 2–4. The cross-section viewpoint has the advantage over top down views because features which are undercut, common for the nodular powder features, can be seen. The nodular and balled features caused by partially fused powder particles are shown for the as-printed surface in Fig. 4a. Similar to the surface images, the electropolished sample in Fig. 4c shows no partially fused powder features and a few dimples (smooth craters on the surface). These surface asperities were again shown to not be completely removed by tumble polished or contour scan/re-melting surface treatment, shown in Fig. 4e, g, respectively.

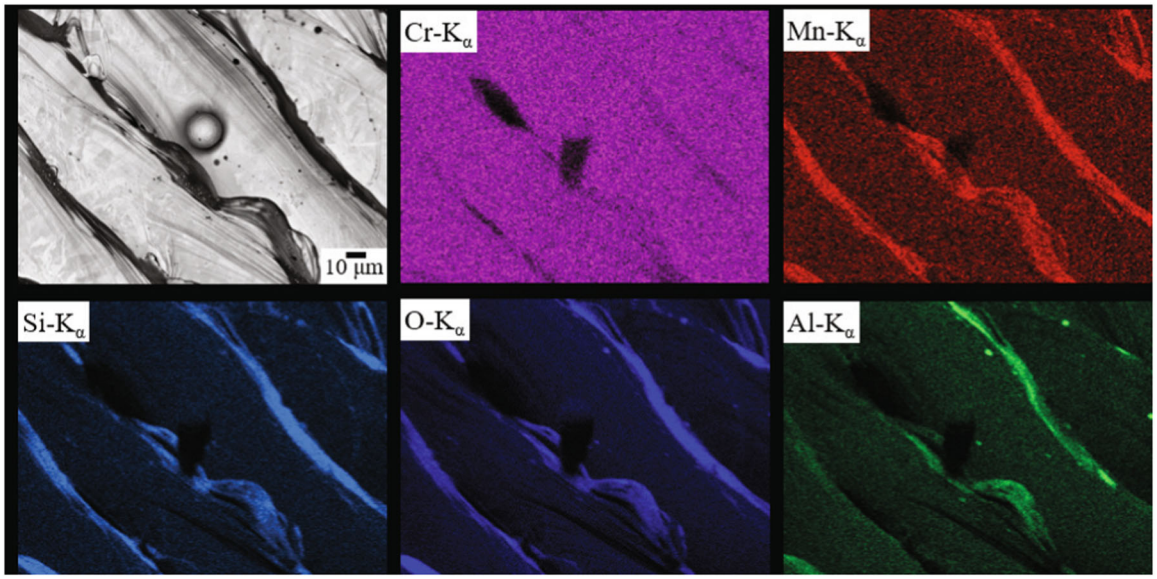

Fig. 5 Chemical map of as-printed surface. BSE image and EDS map of as-printed Top surface showing oxide deposited during PBF process.

Numerous overlapping, sharp, and overhung features can be seen for the as-printed, tumble polished, and contour scan strategy sample cross-sections where the partially fused powder resides, producing small gaps and pockets on the surface. Such features were abundant for the side, upskin, and downskin orientations, while the top orientation was generally free of them. Common for PBF metals, these features have been investigated from the cross-section perspective by others because optical, top down, analysis techniques cannot capture them[52,54]. The areas where metal is overlapping itself may lead to crevice-like corrosion environments, similar to lack of fusion porosity. These regions can increase a parts susceptibility to corrosion initiation and lead to severe localized corrosion, on normally passive metals[7,20].

The inverse pole figure maps for each of these samples show the nodular features to typically have a small grain sizes (<10 μm), shown in Fig. 4b for the as-printed condition, likely derived from the original powder particle microstructure[87]. The bulk AM material, ~50 μm below the surface, shows a typical PBF 316L microstructure with large (>20 μm) elongated, columnar grains and at higher magnifications (not shown), the dislocation cell sub-structure with solute (Cr/Mo) segregation, similar to what others have observed[88]. The pole figure map for the electro-polished sample, in Fig. 4d, shows no signs of the small grained regions verifying the partially fused powder was completely removed during electro-polishing. The contour scan/re-melted specimen in Fig. 4h shows small grains in the partially fused powder, similar to the as-printed sample or from the rapid cooling associated with the re-melting process. The tumble polished sample, in Fig. 4f also exhibits small grains along with heavily deformed regions at the surface (not able to be indexed with EBSD, top left of Fig. 4f) suggesting the partially fused powder was mechanically deformed by the ceramic polishing media.

Local chemical heterogeneities of the as-printed surface were characterized by energy dispersive spectroscopy (EDS) mapping, shown in Fig. 5. This was initially performed because of BSE images showing dark regions corresponding to the interfaces between melt pool tracks or splatter, as shown in Fig. 5a. The EDS maps show these dark regions to primarily consist of Mn, Si, Al, and O, which are also the typical constituents of the nanoscale oxide inclusions dispersed throughout the AM stainless steel microstructures[87,89–91]. These layers of oxygen rich compounds in between each melt pool were observed for all orientations of the as-printed samples as well as for the contour scan strategy and tumble polished specimens. Similar oxygen rich layers were removed by the electro-polishing and grinding processes, not clearly observed in the bulk of the AM specimens, an example of this is shown in Supplementary Fig. 5.

Roughness and electrochemical analysis

To quantify roughness of the AM samples, the areal arithmetic mean height (S_a) and areal peak height (S_z) were measured with a white light interferometer, summarized in Fig. 6. Both surface roughness metrics are commonly used in industry and expected to exhibit quantifiable differences between the different surface treatments, with the S_z metric expected to help identify surfaces with high aspect ratio features (unfused powder). These roughness measurements were performed at the center of 8 samples for each surface finish and build angle. Representative topography maps for the top orientation are shown in Fig. 6a–d with the side, upskin, and downskin orientations shown in the Supplementary Fig. 6. The red colored features shown in Fig. 6a are areas where partially fused powder is present on the surface, which is less noticeable on the other surface finishes in the top orientation. For the other build angles in the Supplementary Fig. 6 similar red features are prominent on the as-printed and contour scan strategy surfaces with the electro-polished and tumble polished showing few tall asperities.

The low number of tall structures in the topography maps tended to correspond with smaller S_a values showing the trend for the S_a measurements, in Fig. 6e, to be as-printed > contour scan/re-melted > tumble polished > electro-polished, for all build angles. The build angle also exhibits a trend with the top orientations showing the smallest S_a values, the side and upskin orientations exhibiting slightly larger and similar S_a values, and the downskin orientations S_a measurements displaying the largest average magnitude for any given surface treatment. These trends do not hold for S_z measurements in Fig. 6f where the only surface finish showing some reduction in S_z values are the electro-polished specimens for the top and upskin orientations, while all other measurements have an S_z value of ~150 μm. This suggests the S_a value is more adept at distinguishing between surfaces different surface topologies while the S_z value will consider all surfaces similar if even one peak and one valley combination from an otherwise smooth surface (electro-polished samples) are on the same length scale as a surface with hundreds of peaks and valleys (as-printed/tumble polished/contour scan/re-melted samples).

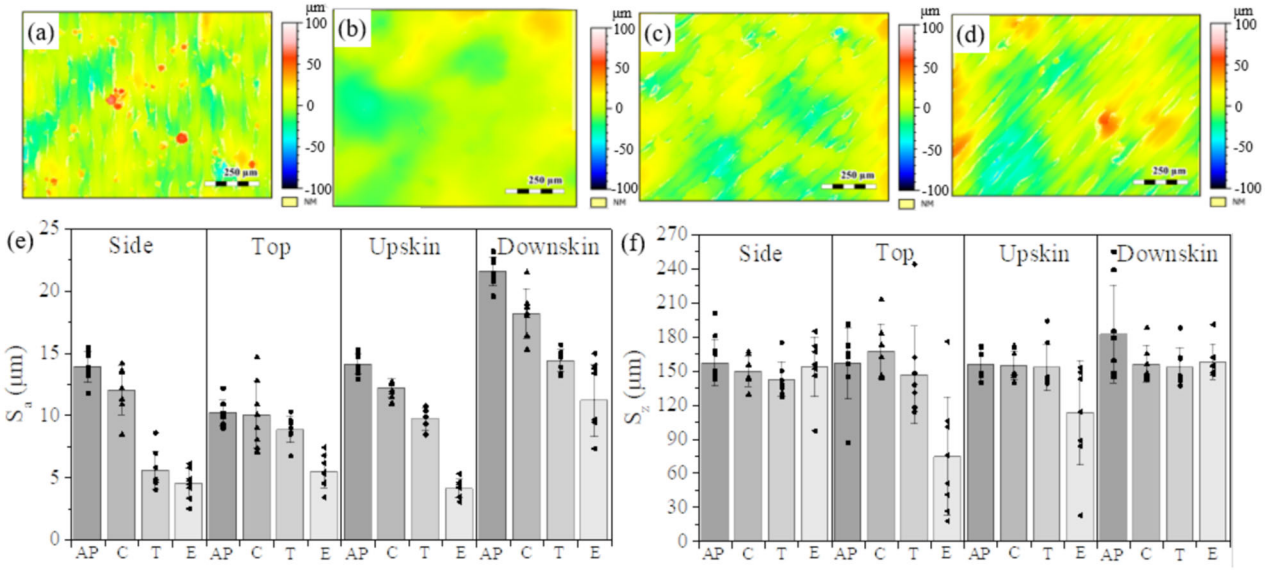

Fig. 6 Surface roughness measurements. Representative white light interferometry measurements of **a** as-printed (AP), **b** electro-polished (E), **c** tumble polished (T), **d** contour scan/re-melting (C) surface treatments with the summary of **e** average surface roughness (S_a), and **f** peak-to-height (S_z) measurements from each surface finish and build angle. Error bars represent one standard deviation while the individual symbols show all data for a given condition to show spread.

Representative potentiodynamic measurements for the top and side orientations and summarized E_b values are shown in Fig. 7. The rougher surface's (as-printed, contour scan/re-melted, tumble polished, passivated) potentiodynamic measurements, presented in Fig. 7a, b, corroborate the mechanism proposed by previous work. Burstein et al. showed an increase in roughness led to easier breakdown of passivity for stainless steel via an increase in number of potential metastable pit initiation sites[36]. The other surface orientations show similar results, in Supplementary Fig. 7. These potentiodynamic measurements show increased metastable pitting activity, i.e. spikes in current density in the passive region, for the rough surface finishes. Similar metastable pitting events were not commonly detected on the smoother electro-polished and ground samples.

Another factor that will impact the breakdown of passivity and increase the likelihood for stabilizing pit growth stems from the Galvele pit stability criterion (x.i)[36,41]. A larger diffusion length (x) for the anolyte, controlled on the rougher surfaces by the sharp overhung features (10–50 μm deep), would require a lower current density (i) to transition a pit from metastable to stable. In Fig. 4 the number of sharp overhung features, which control the severity of the diffusion path, for a given surface finish correlates well with the specimens E_b, with the lowest number of overhung features on the electro-polished sample having the largest E_b. These mechanisms, increased metastable pitting frequency and a lower current density critical to stabilize pitting, are likely the main contributors to the increased pitting susceptibility (low E_b) for the rougher surfaces. Additionally, this pit stability criterion effect can be exacerbated by the development of an occluded differential aeration cell which may occur under open circuit conditions, in real world scenarios, formed in the overhung features on these rough surfaces[7,20,92].

The trend for averaged E_b values in Fig. 7c is generally the opposite compared to the S_a measurements in Fig. 6e, with an increase in E_b as the S_a value is reduced. For every build angle, the electro-polished samples exhibited the largest E_b values (excluding ground) compared to the other surface finishes. All comparisons were made using a two-tailed, unequal variance, Student's t-test with a p-value < 0.05 disproving the null hypothesis. The only exception was the top orientation of the contour scan strategy samples which exhibited a statistically similar (p-value = 0.06) average E_b value to electro-polished in the top orientation. The electro-polished specimen in the side (p-value = 0.41) and upskin (p-value = 0.26) orientations were statistically similar to ground in the same orientation while the top (p-value = 0.04) and downskin (p-value = 1.2×10^{-5}) orientations were statistically different compared to the ground specimens, ground surfaces having a larger E_b than electro-polished samples.

Comparing the orientation dependence of the E_b for a given surface finish, in Fig. 7c, shows the top orientation for as-printed, tumble polished, contour scan strategy/re-melt, and passivated surface conditions are all statistically different (p-value < 0.05) than the other three orientation's E_b. There are two exceptions; comparing the top to the side orientation for the AP and P surface finishes. The electro-polished and ground samples show no statistically significant differences when comparing the top orientation to the other three build angles, suggesting there is no dependence of the as-printed microstructure at different build orientations on the corrosion response when polished to a smooth surface. Additionally, the downskin S_a value for electropolished samples is similar to the side and upskin values for as-printed and contour scan specimens, however, the E_b remains large likely caused by a lack of "cling-on" features.

The relations between S_a/S_z and E_b are plotted in Fig. 8, regardless of build angle. A plateau in E_b is expected at ~1.2 $V_{Ag/AgCl}$, roughly where the ground and electro-polished surface treatment measurements reside. All other surface finishes E_b fall below this plateau, trending to the OCP value (−0.26 to −0.01 $V_{Ag/AgCl}$) of 316L as the S_a/S_z magnitude increases. The trend seen for the S_a vs. E_b plot, Fig. 8a, approaches linearity with moderate correlation ($R^2 = 0.57$) between S_a and E_b. The tumble polished samples act as the largest outliers for the S_a vs. E_b case, exhibiting lower E_b values than expected given their relatively low S_a values. When the tumble polished specimen measurements are removed from the data set, the linear relationship correlation between S_a and E_b becomes stronger ($R^2 = 0.71$). A poor correlation ($R^2 = 0.25$) was found between S_z and E_b, in Fig. 8b, not shown to exhibit the same linear behavior as the S_a vs. E_b, with a cluster of E_b and S_z measurements between 0.0–1.2 $V_{Ag/AgCl}$ and 120–200 μm, respectively.

The E_b of the AM 316L electro-polished and ground surfaces are shown to be statistically larger (p-value < 0.05) than the E_b measurements from wrought 316L samples in Fig. 8. Similar

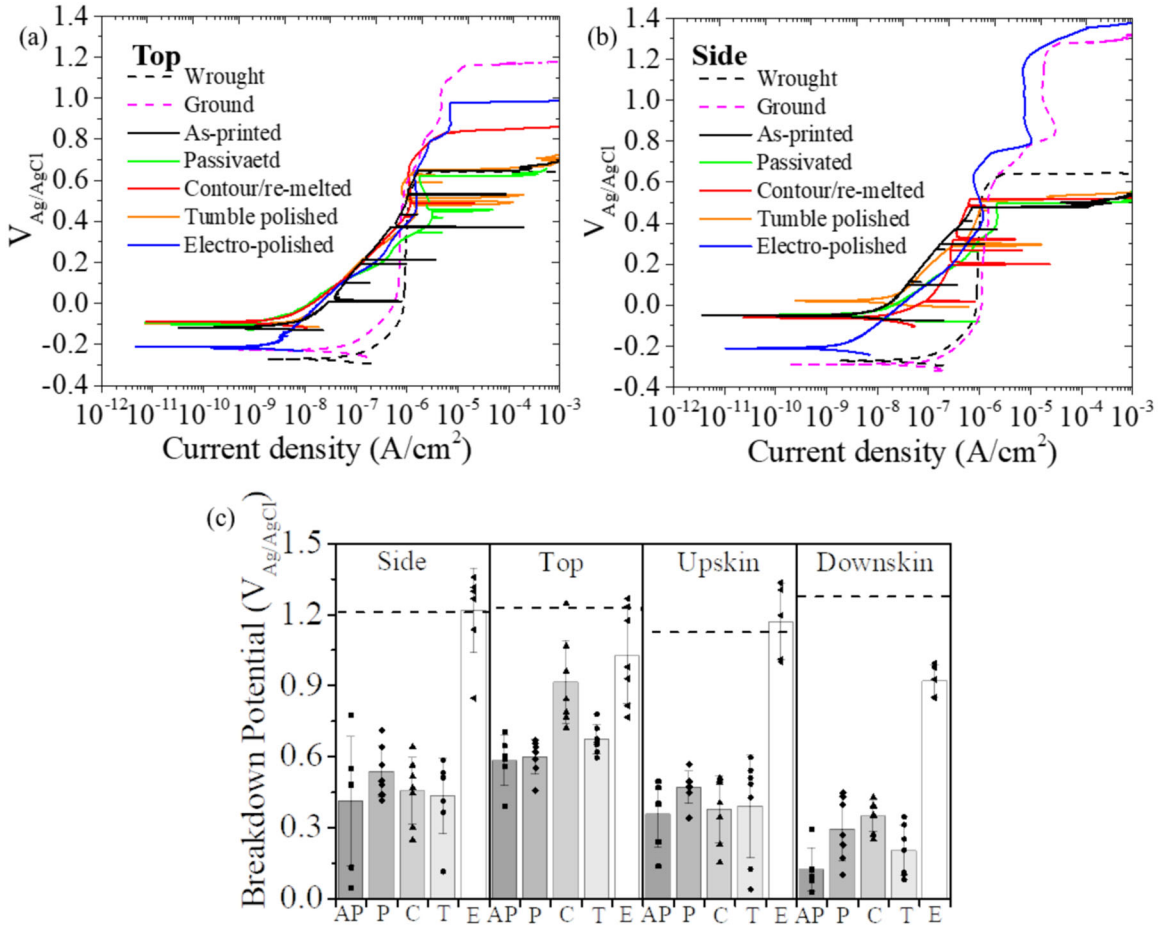

Fig. 7 Breakdown potential measurements. Representative potentiodynamic measurements for all surface treatments in the **a** top and **b** side build angles with the summary of E_b in **c**. Error bars represent one standard deviation while the individual symbols show all data for a given condition to show spread, the data for passivation (P) is also presented. The horizontal dashed lines in **c** represent the average E_b for the ground condition. The E_b measurements for the ground surface of the wrought ground 316L is shown in **a**, **b**.

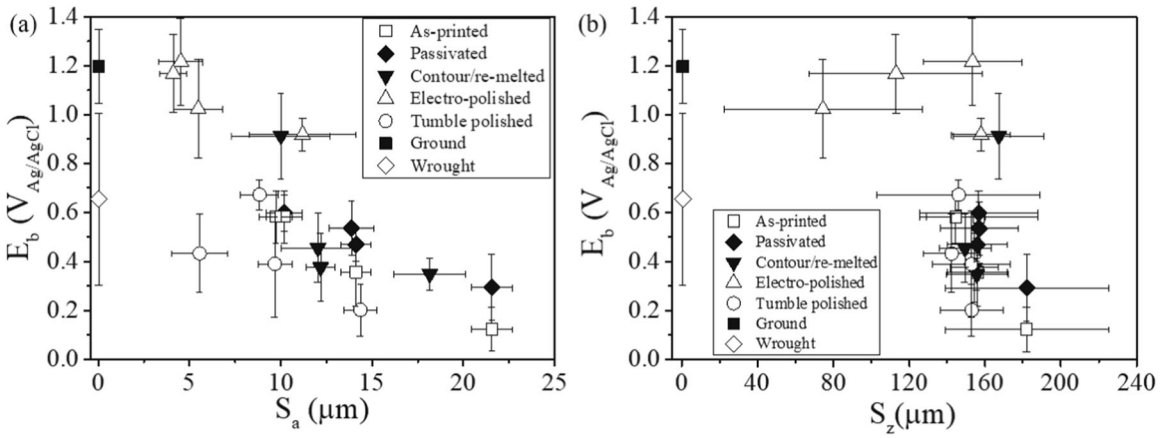

Fig. 8 Relationship between breakdown potential and surface roughness. Scatter plots of E_b with respect to roughness measurements, **a** S_a and **b** S_z. The E_b and roughness measurements for a ground surface of wrought 316L is shown. Error bars represent one standard deviation for all measurements.

results have been observed for other AM/PBF 316L materials[1,9]. The explanation given for the increase in E_b for the AM materials is still under investigation with the suspected reason stemming from a refinement of the non-metallic inclusions, commonly shown to act as pit initiation sites.

Roughness and overhung/cling-on features are portrayed here as the major contributor to passivity breakdown, however several features, elaborated on in the Introduction, associated with the as-printed surface may impact the initiation and propagation of corrosion or other degradation modes (stress corrosion cracking,

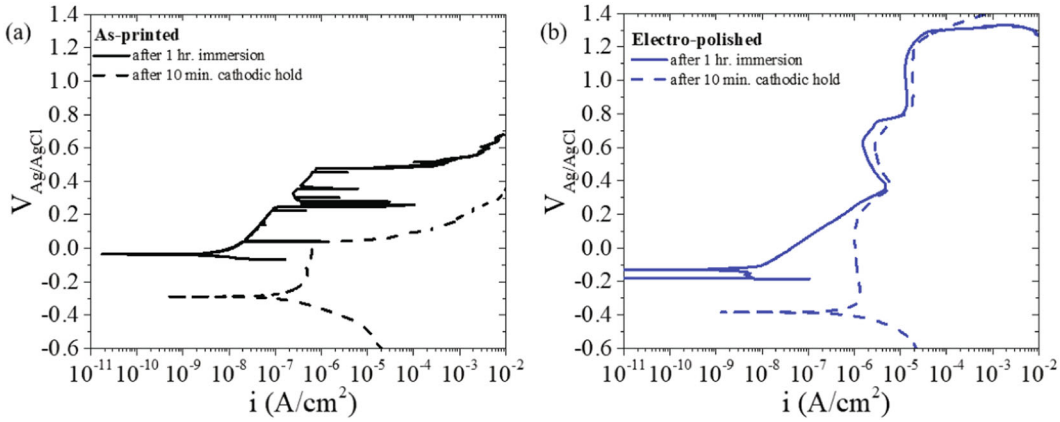

Fig. 9 Breakdown potential after cathodic polarization. Anodic potentiodynamic polarization measurements for **a** as-printed and **b** electro-polished specimens, after a 1 h OCP (solid line) or a cathodic potentiostatic hold at −1.5 $V_{Ag/AgCl}$ (dashed line).

H-embrittlement, mech. fracture, etc.). Microstructural features associated with the partially fused powder, smaller grain size/differing chemical heterogeneities than the bulk, could lead to different electrochemical properties than the fully melted part and exacerbate the local corrosion initiation frequency and in addition to occluded cell effects[93]. Similarly, for tumble polished samples, the deformed layer, if not completely covering the surface, could lead to a local change in OCP caused by cold working of stainless steel, leading to a potential galvanic couple[94,95].

The polarization measurements in Fig. 9 attempt to separate the impact surface oxides, formed at the liquid metal/processing gas interface, have on the E_b from roughness effects. After a cathodic potentiostatic hold (at−1.5 $V_{Ag/AgCl}$ for 10 min), to cathodically reduce Cr and Fe oxides from the surface, a potentiodynamic measurement was performed on an as-printed and electro-polished sample in the side orientation[96,97]. The impact surface oxides had on the potentiodynamic measurements can be seen for both specimen at potentials near OCP, showing order of magnitude reductions in current density signifying the loss of a surface film that was providing some additional passive response (suspected to be Cr/Fe surface oxides formed during processing, NOT the thicker Si/Al/Mn rich oxide shown in Fig. 5).

The as-printed sample after oxide removal (dashed line in Fig. 9a) shows a reduction in E_b compared to the experiment performed without cathodic polarization, suggesting the surface oxides formed during the PBF process have some beneficial effect on the corrosion resistance of the as-printed surface. This change is likely caused by the roughness dominated effects of local corrosion initiation, however there could be several underlying, convoluting factors with respect to roughness effects such as the IR potential drop effects that occur on the rough surface. In contrast, the smoother electro-polished sample in Fig. 9b showed no change in its E_b after oxide removal (assumed to be complete after the 10 min cathodic hold). If the current density shifting to lower values near the E_{corr} indicates complete oxide removal then this is further indication that tortuosity and roughness control, to a first order, the susceptibility of AM metal parts to local corrosion initiation. Fathi et al. observed a similar response for an AM AlSi10Mg alloy, showing the rough as-printed condition to have superior corrosion resistance (larger E_b) compared to a polished specimen at short immersion times in a NaCl solution, suggested to be caused by surface oxides formed during the AM process[35]. However, at longer immersion times the as-printed condition demonstrated lower corrosion resistance than the ground condition, similar to what is shown here.

Implications

The as-printed surface morphology is extremely rough which showed a strong correlation to increased pitting corrosion susceptibility. However, the results from this study are encouraging. Grinding and electro-polishing were viable options for smoothing the surface roughness of flat surfaces, and reducing the susceptibility to pit initiation via the increased E_b to a state superior to wrought 316L. Grinding is not a viable option for polishing complex AM parts, such as truss/lattice structures, in contrast to electro-polishing which remove the tortuous asperities and has the potential to address polishing of complex geometries. Some of these issues for electro-polishing complex shapes are being addressed by other groups such as Urlea et al. They have shown if cathodes are built along side the complex shaped part, creating a custom cathode for each part so electro-polishing can be done more efficiently and hopefully improve the parts tolerance limits[64,65].

The other surface treatment routes in this study provide mixed results. Passivation of the as-printed part was underwhelming, providing minimal increase in E_b. While optimization to the procedures could be made, the primary driving force for increased pit susceptibility continues to be surface topology. Tumble polishing did provide a reduction in S_a, however, the remaining overhung features persisted and likely led to increased pit susceptibility, lower E_b. That said, tumble polishing may be viable with added optimization, possibly increasing the polishing time to remove more material so the tortuous features are completely removed or changing the polishing media to something that more efficiently cleaves high aspect ratio asperities. Finally the contour scan strategy/surface re-melting (without parameter optimization) proved to only significantly improve the corrosion resistance of the top build surface, having minimal impact on the roughness and corrosion behavior of the other build angles[98].

This study investigates how the as-printed surface of powder bed fusion (PBF) 316L stainless steel parts, at four build angles, and several surface finishing treatments (passivation, contour scan strategy/re-melting, tumble polish, electropolish, and planar grinding) impact the surface roughness and susceptibility to initiation of localized corrosion in a quiescent 0.6 M NaCl solution. The major takeaway was an increase in average surface roughness (S_a) resulted in a general decrease in breakdown potential (E_b), suggesting an increased susceptibility to the initiation of localized corrosion for rougher AM metal surfaces. The S_a was build angle dependent, showing a maximum value for the downskin sample orientations and a minimum for the top orientation, regardless of surface finish treatment. This build angle dependence was predicated on the quantity of partially fused powder cling-ons

with the more overhung build surface generally having more partially fused powder. This increase to S_a and amount of partially fused powder also led to a decrease in E_b with the minimum values for all surface finish treatments shown for the downskin orientation. The increased susceptibility to localized corrosion (low E_b) for the rougher surfaces stemmed from an increased metastable pitting frequency and lower current density critical to stabilize pits.

Other key takeaways from this study are the impact from passivation of an as-printed surface minimally impacts the corrosion susceptibility. The addition of a contour scan strategy/surface re-melt did reduce the S_a regardless of build angle, largely reducing the overall number of "cling-on" features. That said these S_a reductions did not significantly impact the E_b. Tumble polishing exhibited large reductions in S_a values, regardless of build angle, with respect to the as-printed surfaces. However, the E_b was not increased significantly with respect to the as-printed samples because tumble polishing failed to remove the tortuous sharp, partially fused powder, features which were the main culprit in causing susceptibility to localized corrosion initiation.

Finally, the electropolishing and planar grinding surface finish treatments provided the largest reductions in S_a and increase to E_b, regardless of surface build angle, for simple shaped AM metal parts. The electro-polishing treatment may provide a robust approach for reducing surface roughness, removing tortuous surface features, and reducing susceptibility to localized corrosion for complex AM metal part designs.

METHODS

Materials and additive manufacturing

The 316L stainless steel powder was provided by (3D Systems). A PBF technique was performed on a 3D Systems ProX DMP 200 to create a total of 48 parallelepiped prism samples on three separate 316L build plates (16 samples per plate). A cross-section schematic of the PBF layered build process is presented in Fig. 1. The processing parameters for all samples are summarized in Table 2, to produce high density (>99%) stainless steel parts. The parallelepiped prism samples were built with a 45° angle to the build plate normal, as shown in Fig. 2a, and an edge length of 1.5 cm. The surface orientations top, side, upskin, and downskin, are labelled in Fig. 2b on an as-printed sample; this nomenclature is taken from previous studies[45,47]. The raster scan pattern for each square layer was rotated 90° every layer, repeating every 5th layer. General chemistry for the PBF 316L parts is shown in Table 3, performed by NSL Analytical Services with inductively coupled plasma— optical emission spectroscopy (ICP-OES) and a LECO Corp. combustion tool.

Surface finish treatments

Initially, 32 of the 48 parallelepiped prism samples (two build plates) were in the as-printed condition. The other 16 samples had a contour scan strategy/re-melting incorporated into the build where after a layer was built, the outer edge was re-melted using a laser power of 33 W and a scan velocity of 160 mm/s prior to covering it with more powder[98]. The use a contour scan strategy is commonly incorporated into scan strategies and an approach to minimize roughness[98–100]. Once the samples were complete, the entire top surface was re-melted using the same scan pattern as the final raster pass. Eight of the AP samples were tumble polished for 3 h in a Burr King vibratory chamber (model M25) at a pulse rate of 2000 per min. Fast cutting ceramic media was used at sizes of, 4 × 4 mm, 4 × 8 mm, and 10 × 10 mm, simultaneously, from Royson Engineering Company.

Prior to applying any additional surface finish treatments or material characterization the as-printed, contour scan strategy, and tumble polished samples were ultra-sonicated for 5 min in a 1 vol% VWR hand soap/ultrapure Millipore water (18.2 MΩ cm) deionized (DI) water solution followed by a 5 min sonication in acetone. Sample were rinsed with methanol and dried with house nitrogen gas.

Eight of the as-printed samples were electropolished. Prior to electropolishing a Cu wire was attached to the samples surface cut from the build plate with silver conductive epoxy adhesive (MG Chemical Ltd., Ontario Canada) and covered with 5 min epoxy (Devcon, Ontario Canada). Electro-polished samples were fully immersed in a solution of 50 vol% phosphoric acid, 20 vol% sulfuric acid, and 30 vol% DI water. A platinized Nb mesh cage was used as the counter electrode which surrounded the 5 exposed faces of the parallelepiped prism. The electro-polishing took place over 12 min at 5 A (4.9 V), which correlates to ~500 mA/cm^2. The polarity was reversed every 2 min, for 10 s, to reduce the oxide formed on the samples during polishing. Anywhere from 10 to 20 µm of material (including the partially fused powder) was removed after the 12 min electro-polishing process. Tumble and electro-polishing of the as-printed samples were chosen as the two approaches with great potential to effectively polish a complex part, post-build[64,82,101,102].

Eight of the AP samples were chemically passivated according to ASTM A967/A967M-17[103]. Each sample was individually immersed in a 45 vol% nitric acid, 55 vol% DI water solution for 30 min followed by a thorough rinse with DI water. Samples were then placed in a solution of 5 wt% NaOH solution at 70 °C for 30 min followed by a 5 min ultra sonication in DI water. The sample was then dried with house nitrogen gas. Passivation was chosen as it is a common surface treatment performed on wrought stainless steels.

After all roughness and electrochemical experiments were performed on the as-printed, contour scan strategy, tumble polished, electro-polished, and passivated samples, six samples were randomly selected from each lot and had all surfaces ground with SiC paper to a 1200 grit finish. Roughness and electrochemical experiments were then performed on the ground samples for all surface orientations.

Surface roughness measurement

Surface roughness measurements for all surface finishes and orientations were taken optically using white light interferometry (Zygo,NexView, USA). The coherence scanning interferometry (CSI) mode was used with a 20x objective lens (1× zoom lens, FOV: 0.42 × 0.42 mm, 0.407 µm lateral resolution). An area (1 × 1 mm) near the center of each surface face was stitched together from ~12 measurements with a 3 × 3 Gaussian denoising filter (no other filters we used). Roughness values corresponding to average surface roughness (S_a) and maximum surface peak/depth (S_z), were extracted from a 1 × 0.75 mm area using the surface metrology software, MountainsMap® V 7.4, according to ISO 25178. Each measurement was corrected for general tilt. All 8 samples for each surface condition were measured.

Electrochemical measurements

Prior to electrochemical measurements a copper wire was connected to the cut surface (build plate) of each sample with silver conductive epoxy, same as for the electro-polishing process. Electrochemical tests were carried out using a standard three electrode cell with a Pt mesh counter electrode and a Ag/AgCl (saturated KCl) reference electrode (+0.197 V vs. SHE).

Table 2. PBF processing parameters.

Laser power (W)	110
Laser velocity (mm/s)	1400
Layer thickness (µm)	30
Laser focus offset (mm)	+1
Average power diameter (µm)	12

Table 3. Composition of 316L as-printed part.

Composition (wt%)	Al	C	Cr	Fe	Mn	Mo	Ni	N	O	P	Si	S
As-printed	0.003 ± 0.0005	0.017 ± 0.003	17.3 ± 0.35	67.2 ± 0.34	1.07 ± 0.12	2.16 ± 0.2	11.1 ± 0.22	0.093 ± 0.014	0.063 ± 0.0094	0.019 ± 0.0029	0.65 ± 0.098	0.009 ± 0.001

A Viton o-ring was attached to the surface of interest with quickset epoxy to reduce the likelihood of crevice corrosion, exacerbated by the rough surfaces. No samples showed signs of crevice corrosion under the epoxy mask. The o-ring was attached to the corrosion cell with quickset epoxy. The exposed area varied from sample to sample and was measured using a Keyence digital microscope and ranged from 0.06 to 0.637 cm^2.

Anodic potentiodynamic polarization measurements were carried out to determine each samples breakdown potential (E_b) on a Biologic VMP300 multichannel potentio/galvanostat. Prior to the potentiodynamic measurement samples were immersed at open circuit potential (OCP) for 1 h in a quiescent 0.6 M NaCl solution at 21 ± 1 °C. The potentiodynamic measurements started 20 mV below the samples OCP and scanned at a rate of 0.167 mV/s in the anodic direction to $+1.5\ V_{Ag/AgCl}$ or the experiment was stopped when a current density of 10^{-2} A/cm^2 was reached. In all, 6–8 tests were carried out for each orientation and for each surface finish.

Anodic potentiodynamic polarization measurements were also carried out after a cathodic potentiostatic hold for select as-printed and electropolished samples in the side orientation. These experiments were used to determine the E_b of surfaces after their surface oxides, which formed during processing, have been removed. The samples were briefly placed at OCP for 10 s and then held for 10 min at a cathodic potential of $-1.5\ V_{Ag/AgCl}$ followed by an anodic potentiodynamic measurement using the same parameters noted above.

Microstructure characterization

Specimens were prepared to observe the microstructure for each build angle surface in cross-section. These specimens were mounted in epoxy and polished to a mirror finish using successively finer SiC grit paper followed by a two-step vibratory polish using a 0.3-μm Al_2O_3 slurry for 24 h followed by a 0.04-μm SiO_2 slurry for 24 h. Scanning electron microscopy (SEM) was used to image, in secondary and backscattered electron imaging modes, the rough surfaces and mounted cross-section samples. A Zeiss Supra 55-VP field emission SEM equipped with an Oxford Instruments X-Max SDD EDS detector and an Oxford Symmetry EBSD was used for all SEM work. A working distance of 10 mm and accelerating voltage of 20 kV were used for all SEM imaging and analysis.

DATA AVAILABILITY

The data that support the findings of this study are available from the corresponding author upon reasonable request.

Received: 14 April 2020; Accepted: 6 July 2020;
Published online: 30 July 2020

REFERENCES

1. Chao, Q. et al. On the enhanced corrosion resistance of a selective laser melted austenitic stainless steel. *Scr. Mater.* **141**, 94–98 (2017).
2. Chen, X., Li, J., Cheng, X., Wang, H. & Huang, Z. Effect of heat treatment on microstructure, mechanical and corrosion properties of austenitic stainless steel 316L using arc additive manufacturing. *Mater. Sci. Eng. A* **315**, 307–314 (2018).
3. Cruz, V. et al. Electrochemical studies on the effect of residual stress on the corrosion of 316L manufactured by selective laser melting. *Corros. Sci.* **164**, 108314 (2019).
4. Kong, D. et al. Heat treatment effect on the microstructure and corrosion behavior of 316L stainless steel fabricated by selective laser melting for proton exchange membrane fuel cells. *Electrochim. Acta.* **276**, 293–303 (2018).
5. Lodhi, M. J. K., Deen, K. M. & Haider, W. Corrosion behavior of additively manufactured 316L stainless steel in acidic media. *Materialia* **2**, 111–121 (2018).
6. Macatangay, D. A., Thomas, S., Birbilis, N. & Kelly, R. G. Unexpected interface corrosion and sensitization susceptibility in additively manufactured austenitic stainless steel. *Corros. J.* **74**, 153–157 (2018).
7. Melia, M. A., Nguyen, H.-D. A., Rodelas, J. M. & Schindelholz, E. J. Corrosion properties of 304L stainless steel made by directed energy deposition additive manufacturing. *Corros. Sci.* **152**, 20–30 (2019).
8. Papula, S. et al. Selective laser melting of duplex stainless steel 2205: effect of post-processing heat treatment on microstructure, mechanical properties, and corrosion resistance. *Materials* **12**, 2468 (2019).
9. Sander, G. et al. On the corrosion and metastable pitting characteristics of 316L stainless steel produced by selective laser melting. *J. Electrochem. Soc.* **164**, C250–C257 (2017).
10. Schaller, R. F., Taylor, J. M., Rodelas, J. & Schindelholz, E. J. Corrosion properties of powder bed fusion additively manufactured 17-4 PH stainless steel. *CORROSION* **73**, 796–807 (2017).
11. Trelewicz, J. R., Halada, G. P., Donaldson, O. K. & Manogharan, G. Microstructure and corrosion resistance of laser additively manufactured 316L stainless steel. *JOM* **68**, 850–859 (2016).
12. Wang, Y. & Chen, X. Investigation on the microstructure and corrosion properties of Inconel 625 alloy fabricated by wire arc additive manufacturing. *Mater. Res. Express* **6**, 106568 (2019).
13. Kubacki, G. W., Brownhill, J. P. & Kelly, R. G. Comparison of atmospheric corrosion of additively manufactured and cast Al-10Si-Mg over a range of heat treatments. *CORROSION* **75**, 1527–1540 (2019).
14. Revilla, R. I., Liang, J., Godet, S. & De Graeve, I. Local corrosion behavior of additive manufactured AlSiMg alloy assessed by SEM and SKPFM. *J. Electrochem. Soc.* **164**, C27–C35 (2017).
15. Zhang, B., Xiu, M., Tan, Y. T., Wei, J. & Wang, P. Pitting corrosion of SLM Inconel 718 sample under surface and heat treatments. *Appl. Surf. Sci.* **490**, 556–567 (2019).
16. Stoudt, M. R., Ricker, R. E., Lass, E. A. & Levine, L. E. Influence of postbuild microstructure on the electrochemical behavior of additively manufactured 17-4 PH stainless steel. *JOM* **69**, 506–515 (2017).
17. Sander, G. et al. Corrosion of additively manufactured alloys: a review. *CORROSION* **74**, 1318–1350 (2018).
18. Cabrini, M. et al. Evaluation of corrosion resistance of alloy 625 obtained by laser powder bed fusion. *J. Electrochem. Soc.* **166**, C3399–C3408 (2019).
19. Kazemipour, M., Mohammadi, M., Mfoumou, E. & Nasiri, A. M. Microstructure and corrosion characteristics of selective laser-melted 316L stainless steel: the impact of process-induced porosities. *JOM* **71**, 3230–3240 (2019).
20. Schaller, R. F., Mishra, A., Rodelas, J. M., Taylor, J. M. & Schindelholz, E. J. The role of microstructure and surface finish on the corrosion of selective laser melted 304L. *J. Electrochem. Soc.* **165**, C234–C242 (2018).
21. Ni, X. et al. Corrosion behavior of 316L stainless steel fabricated by selective laser melting under different scanning speeds. *J. Mater. Eng. Perform.* **27**, 3667–3677 (2018).
22. Mohd Yusuf, S., Nie, M., Chen, Y., Yang, S. & Gao, N. Microstructure and corrosion performance of 316L stainless steel fabricated by selective laser melting and processed through high-pressure torsion. *J. Alloy. Compd.* **763**, 360–375 (2018).
23. Kong, D. et al. The passivity of selective laser melted 316L stainless steel. *Appl. Surf. Sci.* **504**, 144495 (2020).
24. Kong, D. et al. Mechanical properties and corrosion behavior of selective laser melted 316L stainless steel after different heat treatment processes. *J. Mater. Sci. Technol.* **35**, 1499–1507 (2019).
25. Prieto, C., Singer, M., Cyders, T. & Young, D. Investigation of pitting corrosion initiation and propagation of a type 316L stainless steel manufactured by the direct metal laser sintering process. *CORROSION* **75**, 140–143 (2018).
26. Cabrini, M. et al. Corrosion behavior of AlSi10Mg alloy produced by laser powder bed fusion under chloride exposure. *Corros. Sci.* **152**, 101–108 (2019).
27. Gharbi, O. et al. Microstructure and corrosion evolution of additively manufactured aluminium alloy AA7075 as a function of ageing. *npj Mater. Degrad.* **3**, 40 (2019).
28. Lou, X., Andresen, P. L. & Rebak, R. B. Oxide inclusions in laser additive manufactured stainless steel and their effects on impact toughness and stress corrosion cracking behavior. *J. Nucl. Mater.* **499**, 182–190 (2018).
29. Sun, S.-H. et al. Excellent mechanical and corrosion properties of austenitic stainless steel with a unique crystallographic lamellar microstructure via selective laser melting. *Scr. Mater.* **159**, 89–93 (2019).
30. Hemmasian Ettefagh, A. & Guo, S. Electrochemical behavior of AISI316L stainless steel parts produced by laser-based powder bed fusion process and the effect of post annealing process. *Addit. Manuf.* **22**, 153–156 (2018).
31. Dai, N. et al. Distinction in corrosion resistance of selective laser melted Ti-6Al-4V alloy on different planes. *Corros. Sci.* **111**, 703–710 (2016).
32. Leon, A. & Aghion, E. Effect of surface roughness on corrosion fatigue performance of AlSi10Mg alloy produced by Selective Laser Melting (SLM). *Mater. Charact.* **131**, 188–194 (2017).
33. Ni, C., Shi, Y. & Liu, J. Effects of inclination angle on surface roughness and corrosion properties of selective laser melted 316L stainless steel. *Mater. Res. Express* **6**, 036505 (2018).
34. Fathi, P., Rafieazad, M., Duan, X., Mohammadi, M. & Nasiri, A. M. On microstructure and corrosion behaviour of AlSi10Mg alloy with low surface roughness fabricated by direct metal laser sintering. *Corros. Sci.* **157**, 126–145 (2019).
35. Fathi, P., Mohammadi, M., Duan, X. & Nasiri, A. M. Effects of surface finishing procedures on corrosion behavior of DMLS-AlSi10Mg_200C alloy versus die-cast A360.1 aluminum. *JOM* **71**, 1748–1759 (2019).
36. Burstein, G. T. & Pistorius, P. C. Surface roughness and the metastable pitting of stainless steel in chloride solutions. *CORROSION* **51**, 380–385 (1995).

37. Hong, T. & Nagumo, M. Effect of surface roughness on early stages of pitting corrosion of Type 301 stainless steel. *Corros. Sci.* **39**, 1665–1672 (1997).
38. Lee, S. M., Lee, W. G., Kim, Y. H. & Jang, H. Surface roughness and the corrosion resistance of 21Cr ferritic stainless steel. *Corros. Sci.* **63**, 404–409 (2012).
39. Sasaki, K. & Burstein, G. T. The generation of surface roughness during slurry erosion-corrosion and its effect on the pitting potential. *Corros. Sci.* **38**, 2111–2120 (1996).
40. Bagehorn, S., Wehr, J. & Maier, H. J. Application of mechanical surface finishing processes for roughness reduction and fatigue improvement of additively manufactured Ti-6Al-4V parts. *Int. J. Fatigue* **102**, 135–142 (2017).
41. Galvele, J. R. Tafel's law in pitting corrosion and crevice corrosion susceptibility. *Corros. Sci.* **47**, 3053–3067 (2005).
42. Aboulkhair, N. T., Maskery, I., Tuck, C., Ashcroft, I. & Everitt, N. M. Improving the fatigue behaviour of a selectively laser melted aluminium alloy: Influence of heat treatment and surface quality. *Mater. Des.* **104**, 174–182 (2016).
43. Denti, L., Bassoli, E., Gatto, A., Santecchia, E. & Mengucci, P. Fatigue life and microstructure of additive manufactured Ti6Al4V after different finishing processes. *Mater. Sci. Eng., A* **755**, 1–9 (2019).
44. Shrestha, R., Simsiriwong, J. & Shamsaei, N. Fatigue behavior of additive manufactured 316L stainless steel parts: effects of layer orientation and surface roughness. *Addit. Manuf.* **28**, 23–38 (2019).
45. Tian, Y., Tomus, D., Rometsch, P. & Wu, X. Influences of processing parameters on surface roughness of Hastelloy X produced by selective laser melting. *Addit. Manuf.* **13**, 103–112 (2017).
46. Dutta, B., Babu, S. & Jared, B. H. *Science, Technology and Applications of Metals in Additive Manufacturing*. (Elsevier Science, 2019).
47. Townsend, A., Senin, N., Blunt, L., Leach, R. K. & Taylor, J. S. Surface texture metrology for metal additive manufacturing: a review. *Precis. Eng.* **46**, 34–47 (2016).
48. Wang, D., Mai, S., Xiao, D. & Yang, Y. Surface quality of the curved overhanging structure manufactured from 316-L stainless steel by SLM. *Int. J. Adv. Manuf. Syst.* **86**, 781–792 (2016).
49. Qiu, C. et al. On the role of melt flow into the surface structure and porosity development during selective laser melting. *Acta Mater.* **96**, 72–79 (2015).
50. Strano, G., Hao, L., Everson, R. M. & Evans, K. E. Surface roughness analysis, modelling and prediction in selective laser melting. *J. Mater. Process. Technol.* **213**, 589–597 (2013).
51. Grimm, T., Wiora, G. & Witt, G. Characterization of typical surface effects in additive manufacturing with confocal microscopy. *Surf. Topogr.: Metrol. Prop.* **3**, 014001 (2015).
52. Cabanettes, F. et al. Topography of as built surfaces generated in metal additive manufacturing: a multi scale analysis from form to roughness. *Precis. Eng.* **52**, 249–265 (2018).
53. Fox, J. C., Moylan, S. P. & Lane, B. M. Effect of process parameters on the surface roughness of overhanging structures in laser powder bed fusion additive manufacturing. *Proced. CIRP* **45**, 131–134 (2016).
54. Whip, B., Sheridan, L. & Gockel, J. The effect of primary processing parameters on surface roughness in laser powder bed additive manufacturing. *Int. J. Adv. Manuf. Syst.* **103**, 4411–4422 (2019).
55. Bean, G. E., Witkin, D. B., McLouth, T. D., Patel, D. N. & Zaldivar, R. J. Effect of laser focus shift on surface quality and density of Inconel 718 parts produced via selective laser melting. *Addit. Manuf.* **22**, 207–215 (2018).
56. Koutiri, I., Pessard, E., Peyre, P., Amlou, O. & De Terris, T. Influence of SLM process parameters on the surface finish, porosity rate and fatigue behavior of as-built Inconel 625 parts. *J. Mater. Process. Technol.* **255**, 536–546 (2018).
57. Fox, J. C., Kim, F. H., Reese, Z. C. & Evans, C. In (eds Taylor, J. A. & Leach, R.), *2018 ASPE and euspen Summer Topical Meeting - Advancing Precision in Additive Manufacturing* (2018).
58. Kim, F. H., Moylan, S. P., Garboczi, E. J. & Slotwinski, J. A. Investigation of pore structure in cobalt chrome additively manufactured parts using X-ray computed tomography and three-dimensional image analysis. *Addit. Manuf.* **17**, 23–38 (2017).
59. Alrbaey, K., Wimpenny, D. I., Al-Barzinj, A. A. & Moroz, A. Electropolishing of re-melted SLM stainless steel 316L parts using deep eutectic solvents. *J. Mater. Eng. Perform.* **25**, 2836–2846 (2016)
60. Baicheng, Z. et al. Study of selective laser melting (SLM) Inconel 718 part surface improvement by electrochemical polishing. *Mater. Des.* **116**, 531–537 (2017).
61. Rotty, C., Mandroyan, A., Doche, M. L. & Hihn, J. Y. Electropolishing of CuZn brasses and 316L stainless steels: Influence of alloy composition or preparation process (ALM vs. standard method). *Surf. Coat. Technol.* **307**, 125–135 (2016).
62. Rotty, C. et al. Electrochemical superfinishing of cast and ALM 316L stainless steels in deep eutectic solvents: surface microroughness evolution and corrosion resistance. *J. Electrochem. Soc.* **166**, C468–C478 (2019).
63. ur Rahman, Z., Deen, K. M., Cano, L. & Haider, W. The effects of parametric changes in electropolishing process on surface properties of 316L stainless steel. *Appl. Surf. Sci.* **410**, 432–444 (2017).
64. Urlea, V. & Brailovski, V. Electropolishing and electropolishing-related allowances for IN625 alloy components fabricated by laser powder-bed fusion. *Int. J. Adv. Manuf. Syst.* **92**, 4487–4499 (2017).
65. Urlea, V. & Brailovski, V. Electropolishing and electropolishing-related allowances for powder bed selectively laser-melted Ti-6Al-4V alloy components. *J. Mater. Process. Technol.* **242**, 1–11 (2017).
66. Wu, Y.-C., Kuo, C.-N., Chung, Y.-C., Ng, C.-H. & Huang, J. C. Effects of electropolishing on mechanical properties and bio-corrosion of Ti6Al4V fabricated by electron beam melting additive manufacturing. *Materials* **12**, 1466 (2019).
67. Zhang, Y. et al. Amorphous alloy strengthened stainless steel manufactured by selective laser melting: enhanced strength and improved corrosion resistance. *Scr. Mater.* **148**, 20–23 (2018).
68. Wang, W. J., Yung, K. C., Choy, H. S., Xiao, T. Y. & Cai, Z. X. Effects of laser polishing on surface microstructure and corrosion resistance of additive manufactured CoCr alloys. *Appl. Surf. Sci.* **443**, 167–175 (2018).
69. Bhaduri, D. et al. Laser polishing of 3D printed mesoscale components. *Appl. Surf. Sci.* **405**, 29–46 (2017).
70. Bordatchev, E. V., Hafiz, A. M. K. & Tutunea-Fatan, O. R. Performance of laser polishing in finishing of metallic surfaces. *Int. J. Adv. Manuf. Technol.* **73**, 35–52 (2014).
71. Hackel, L., Rankin, J. R., Rubenchik, A., King, W. E. & Matthews, M. Laser peening: a tool for additive manufacturing post-processing. *Addit. Manuf.* **24**, 67–75 (2018).
72. Rosa, B., Mognol, P. & Hascoët, J.-y Laser polishing of additive laser manufacturing surfaces. *J. Laser Appl.* **27**, S29102 (2015).
73. Tian, Y. et al. Material interactions in laser polishing powder bed additive manufactured Ti6Al4V components. *Addit. Manuf.* **20**, 11–22 (2018).
74. Yung, K. C., Xiao, T. Y., Choy, H. S., Wang, W. J. & Cai, Z. X. Laser polishing of additive manufactured CoCr alloy components with complex surface geometry. *J. Mater. Process. Technol.* **262**, 53–64 (2018).
75. Kumbhar, N. N. & Mulay, A. V. Post processing methods used to improve surface finish of products which are manufactured by additive manufacturing technologies: a review. *J. Inst. Eng. (India) Ser. C.* **99**, 481–487 (2018).
76. Pacquentin, W., Caron, N. & Oltra, R. Effect of microstructure and chemical composition on localized corrosion resistance of a AISI 304L stainless steel after nanopulsed-laser surface melting. *Appl. Surf. Sci.* **356**, 561–573 (2015).
77. Boschetto, A., Bottini, L. & Veniali, F. Surface roughness and radiusing of Ti6Al4V selective laser melting-manufactured parts conditioned by barrel finishing. *Int. J. Adv. Manuf. Syst.* **94**, 2773–2790 (2018).
78. Mohammadian, N., Turenne, S. & Brailovski, V. Surface finish control of additively-manufactured Inconel 625 components using combined chemical-abrasive flow polishing. *J. Mater. Process. Technol.* **252**, 728–738 (2018).
79. Nagalingam, A. P. & Yeo, S. H. Controlled hydrodynamic cavitation erosion with abrasive particles for internal surface modification of additive manufactured components. *Wear* **414–415**, 89–100 (2018).
80. Tan, K. L. & Yeo, S. H. Surface modification of additive manufactured components by ultrasonic cavitation abrasive finishing. *Wear* **378–379**, 90–95 (2017).
81. Żebrowski, R. & Walczak, M. The effect of shot peening on the corrosion behaviour of Ti-6Al-4V alloy made by DMLS. *Adv. Mater. Sci* **18**, 43 (2018).
82. Jamal, M. & Morgan, M. N. Design process control for improved surface finish of metal additive manufactured parts of complex build geometry. *Inventions* **2**, 36 (2017).
83. Persenot, T., Martin, G., Dendievel, R., Buffiére, J.-Y. & Maire, E. Enhancing the tensile properties of EBM as-built thin parts: effect of HIP and chemical etching. *Mater. Charact.* **143**, 82–93 (2018).
84. Łyczkowska, E., Szymczyk, P., Dybała, B. & Chlebus, E. Chemical polishing of scaffolds made of Ti–6Al–7Nb alloy by additive manufacturing. *Arch. Civ. Mech. Eng.* **14**, 586–594 (2014).
85. Longhitano, G. A., Larosa, M. A., Munhoz, A. L. J., Zavaglia, C. Ad. C. & Ierardi, M. C. F. Surface finishes for Ti-6Al-4V alloy produced by direct metal laser sintering. *Mater. Res.* **18**, 838–842 (2015).
86. Guo, J. et al. On the machining of selective laser melting CoCrFeMnNi high-entropy alloy. *Mater. Des.* **153**, 211–220 (2018).
87. Heiden, M. J. et al. Evolution of 316L stainless steel feedstock due to laser powder bed fusion process. *Addit. Manuf.* **25**, 84–103 (2019).
88. Birnbaum, A. J., Steuben, J. C., Barrick, E. J., Iliopoulos, A. P. & Michopoulos, J. G. Intrinsic strain aging, Σ3 boundaries, and origins of cellular substructure in additively manufactured 316L. *Addit. Manuf.* **29**, 100784 (2019).
89. Saeidi, K. *Stainless steels fabricated by laser melting: Scaled-down structural hierarchies and microstructural heterogeneities.* (Stockholm University, 2016).
90. Saeidi, K., Kvetková, L., Lofaj, F. & Shen, Z. Austenitic stainless steel strengthened by the in situ formation of oxide nanoinclusions. *RSC Adv.* **5**, 20747–20750 (2015).
91. Simonelli, M. et al. A study on the laser spatter and the oxidation reactions during selective laser melting of 316L stainless steel, Al-Si10-Mg, and Ti-6Al-4V. *Metall. Mater. Trans. A* **46A**, 3842–3851 (2015).

92. Jones, D. A. *Principles and Prevention of Corrosion*. (Prentice Hall, 1996).
93. Abbasi Aghuy, A., Zakeri, M., Moayed, M. H. & Mazinani, M. Effect of grain size on pitting corrosion of 304L austenitic stainless steel. *Corros. Sci.* **94**, 368–376 (2015).
94. Nazarov, A., Vivier, V., Vucko, F. & Thierry, D. Effect of tensile stress on the passivity breakdown and repassivation of AISI 304 stainless steel: a scanning kelvin probe and scanning electrochemical microscopy study. *J. Electrochem. Soc.* **166**, C3207–C3219 (2019).
95. Luo, H., Su, H., Ying, G., Dong, C. & Li, X. Effect of cold deformation on the electrochemical behaviour of 304L stainless steel in contaminated sulfuric acid environment. *Appl. Surf. Sci.* **425**, 628–638 (2017).
96. Kocijan, A. Donik, Č. & Jenko, M. Electrochemical and XPS studies of the passive film formed on stainless steels in borate buffer and chloride solutions. *Corros. Sci.* **49**, 2083–2098 (2007).
97. Pourbaix, M. *Atlas of electrochemical equilibria in aqueous solutions*. (National Association of Corrosion Engineers, 1974).
98. Kummert, C. & Schmid, H.-J. In (ed. Beaman, J. J., Bourell, D. L., Crawford, R. H., Fish, S. & Seepersad, C. C.), *Proc. 29th Annual International Solid Freeform Fabrication Symposium* (2018).
99. Antonysamy, A. A., Meyer, J. & Prangnell, P. B. Effect of build geometry on the β-grain structure and texture in additive manufacture of Ti6Al4V by selective electron beam melting. *Mater. Charact.* **84**, 153–168 (2013).
100. Ortiz Rios, C., Amine, T. & Newkirk, J. W. Tensile behavior in selective laser melting. *Int. J. Adv. Manuf. Syst.* **96**, 1187–1194 (2018).
101. Rotty, C. et al. Comparison of electropolishing behaviours of TSC, ALM and cast 316L stainless steel in H3PO4/H2SO4. *Surf. Inter.* **6**, 170–176 (2017).
102. Hashimoto, F. et al. Abrasive fine-finishing technology. *CIRP Ann.* **65**, 597–620 (2016).
103. International, A. in *ASTM A967/ASTM A967M-17 Standard Specification for Chemical Passivation Treatments for Stainless Steel Parts* (ASTM International, West Conshohocken, 2017).

ACKNOWLEDGEMENTS

We wish to thank C. A. Profazi, C. E. Jaramillo, D. P. Cummings, and S. Dickens for materials preparation and characterization. This study was supported by the Joint Munitions Program between the Department of Defense and Department of Energy, the Aging and Lifetime program, and the ACT AM Materials program. Sandia National Laboratories is a multimission laboratory managed and operated by National Technology and Engineering Solutions of Sandia LLC, a wholly owned subsidiary of Honeywell International Inc. for the U.S. Department of Energy's National Nuclear Security Administration under contract DE-NA0003525.

AUTHOR CONTRIBUTIONS

M.M., E.S., and B.J. designed the sample specimens and overall project plan. J.K. and D.S. printed the stainless steel parts as well as performed tumble polishing. M.M. and J.D. performed all other post-build surface treatments, corrosion experiments, and data interpretation. M.M. wrote a majority of the manuscript with help editing from J.D. and E.S. All authors revised and approved the final paper.

COMPETING INTERESTS

The authors declare no competing interests.

ADDITIONAL INFORMATION

Supplementary information is available for this paper at https://doi.org/10.1038/s41529-020-00126-5.

Correspondence and requests for materials should be addressed to M.A.M.

Reprints and permission information is available at http://www.nature.com/reprints

Publisher's note Springer Nature remains neutral with regard to jurisdictional claims in published maps and institutional affiliations.